Surface & Coatings Technology 321 (2017) 136–145

Contents lists available at ScienceDirect

Surface & Coatings Technology

journal homepage: www.elsevier.com/locate/surfcoat

Fabrication of Ni-Ti-O nanoporous film on NiTi alloy in ethylene glycol containing NaCl

Ruiqiang Hang [a,*], Yanlian Liu [a], Ang Gao [b], Mingxiang Zong [a], Long Bai [a], Xiangyu Zhang [a], Xiaobo Huang [a], Bin Tang [a,*], Paul K. Chu [b]

[a] Research Institute of Surface Engineering, Taiyuan University of Technology, Taiyuan 030024, China
[b] Department of Physics and Materials Science, City University of Hong Kong, Tat Chee Avenue, Kowloon, Hong Kong, China

ARTICLE INFO

Article history:
Received 25 January 2017
Revised 29 March 2017
Accepted in revised form 15 April 2017
Available online 17 April 2017

Keywords:
Anodization
Nickel-titanium alloy
Nanoporous film
Corrosion
Cytocompatibility

ABSTRACT

Ni-Ti-O nanoporous film with pore diameters of 60–75 nm are produced anodically on NiTi in ethylene glycol containing 5–10 vol% H_2O and 0.15–0.3 M NaCl at 10–20 V. The film fabricated in the NaCl-containing electrolyte are much thinner than those prepared in the HCl-containing electrolyte under similar experimental conditions, implying proper amount of H^+ in the electrolyte accelerates formation of the nanopores. Moreover, the experimental conditions to grow Ni-Ti-O nanoporous film on NiTi are not proper for pure Ti and Ni. The film of 1.9 μm in thickness exhibits good cytocompatibility thus is suitable for biomedical applications.

1. Introduction

Anodization is a common surface treatment technique for valve metals and their alloys [1]. In 1999, Zwilling and co-workers found that TiO_2 nanotubes (NTs) could be prepared and self-organized on titanium (Ti) by anodization in a fluoride (F)-containing aqueous electrolyte [2]. The combination of the unique structure and favorable properties of TiO_2 such as biocompatibility, corrosion resistance, and electronic properties has spurred many applications such as dye-sensitized solar cells (DSSCs) [3], gas sensors [4], biosensors [5], photocatalytic hydrogen evolution [6], lithium-ion batteries [7], photocatalytic conversion [8], as well as biomedical coatings [9]. In order to enhance the surface properties and extend the application of the materials, elemental doping has been adopted during anodization of Ti alloys [10]. Under optimal conditions, well-defined nanotubular/porous structures composed of mixed oxides were prepared on TiZr [11], TiTa [12], TiPt [13], TiAu [14], TiNi [15,16], TiRu [17], TiCu [18,19], TiW [20], TiAg [21,22], TiMo [23], and TiAlV [24] alloys. Some of the mixed oxides possess improved and/or new properties compared to TiO_2 TNs. For example, H_2 production on TiO_2 NTs doped with 0.2 at.% Au has been shown to be 30 times higher than that on the bare materials [14] and Ag_2O doped TiO_2 NTs possessed potent and long-term antibacterial ability by continuously releasing Ag^+ ions [21].

It is of scientific and technological interest to investigate the anodization behavior of nearly equiatomic NiTi alloy because it is not only widely used as biomaterials but also Ni may introduce improved properties in some industrial applications. Well-defined Ni-Ti-O NTs have been prepared anodically on NiTi alloy by Kim and co-workers in ethylene glycol (EG) mixed with small amounts of H_2O and NH_4F and the NTs were attractive as electrodes in supercapacitors [25]. Subsequent work showed that Ni-Ti-O NTs could be used as electrodes in electrocatalysis [26], gas [27] and glucose sensors [28], as well as biomedical coatings [15,29–31]. However, all of the works used F^- as the etching ions to fabricate the NTs and the tube length was normally less than 800 nm.

Besides F^-, Cl^- has also been used as etching ions to fabricate TiO_2 NTs on pure Ti by anodization [32–34]. Inspired by these findings, our previous work has successfully grown ordered Ni-Ti-O nanoporous film (NPF) with thickness of 160 μm on the surface of NiTi alloy in the electrolyte composed of EG, H_2O, and HCl [35]. Anodic growth of the NPF may be ascribed to a balance between oxide growth and etching of the oxide by Cl^- under an applied electric field. However, the role played by H^+ and whether it is specific to NiTi is unclear. Herein, to address these issues and determine the specific role of Cl^- in anodization, HCl is substituted by NaCl in the anodization of NiTi alloy as well as pure Ti and Ni. The influence of anodization on the corrosion behavior, Ni release, and cytocompatibility of NiTi alloy is also studied.

2. Experimental details

2.1. Sample preparation

NiTi alloy sheets (Xi'an Saite, China) with 50.8 at.% Ni and dimensions of Φ9.0 mm × 2 mm were used as substrates. Each sample was

* Corresponding authors.
E-mail addresses: hangruiqiang@tyut.edu.cn (R. Hang), tangbin@tyut.edu.cn (B. Tang).

http://dx.doi.org/10.1016/j.surfcoat.2017.04.036
0257-8972/

ground and polished to a mirror finish. The non-working surface was sealed with silicone rubber after a copper wire was attached to the back. Anodization was performed using a power supply (IT6123, ITECH, China) under a constant voltage mode in a 250 ml two-electrode cell with a platinum (Pt) sheet (10 mm × 10 mm × 0.2 mm) as the cathode and the NiTi sheet as the anode at room temperature. The electrolyte with a volume of 100 ml composed of EG, H_2O, and NaCl was used for each sample. The key processing parameters, namely the anodization voltage, H_2O and NaCl concentrations in EG, and anodization time were varied to investigate their respective influence on the anodic behavior of the NiTi alloy. To investigate the role of H^+ in anodization of the NiTi alloy, the NaCl and HCl concentrations in the electrolyte were the same and the same experimental conditions were used to prepare the Ni-Ti-O NPF. The influence of the electrolyte on the anodic growth of NPF on the NiTi alloy was studied by comparing to anodization of pure Ti and Ni under the same conditions. The anodization time was 10 min unless otherwise stated.

2.2. Sample characterization

A field-emission scanning electron microscope (FE-SEM, JSM-7001F, JEOL) equipped with an energy-dispersive X-ray spectrometry (EDS, QX200, Bruker) was used to examine the morphology and determine the elemental composition. High-resolution transmission electron microscopy (HR-TEM, Tecnai F30, FEI) was also performed to determine the microstructure of the NPF.

2.3. Corrosion and Ni release tests

The corrosion behavior was evaluated on an electrochemical workstation (CS350, CorrTest, China) by potentiodynamic polarization at 37 ± 0.1 °C in 50 ml of phosphate buffered solution (PBS, pH = 7.4). The composition of PBS can be found elsewhere [29]. A three-electrode system consisting of a platinum foil (counter electrode), saturated calomel electrode (SCE, reference electrode), and anodized sample (working electrode) was employed. After immersion in PBS for 2 h, the polarization curve was recorded over a potential range of −0.8 V to 1.5 V relative to SCE at a constant scanning rate of 1 mV/s. The corrosion potential (E_{corr}), corrosion current density (I_{corr}), and cathodic Tafel slope (β_c) of each sample were obtained based on the Tafel extrapolation method.

To evaluate the Ni release behavior of the different anodized samples, each anodized sample was immersed in 3 ml of PBS and incubated at 37 ± 0.3 °C for 24 h. The Ni concentration in each solution was determined by inductively-coupled plasma mass spectrometry (ICP-MS, 7500, Agilent).

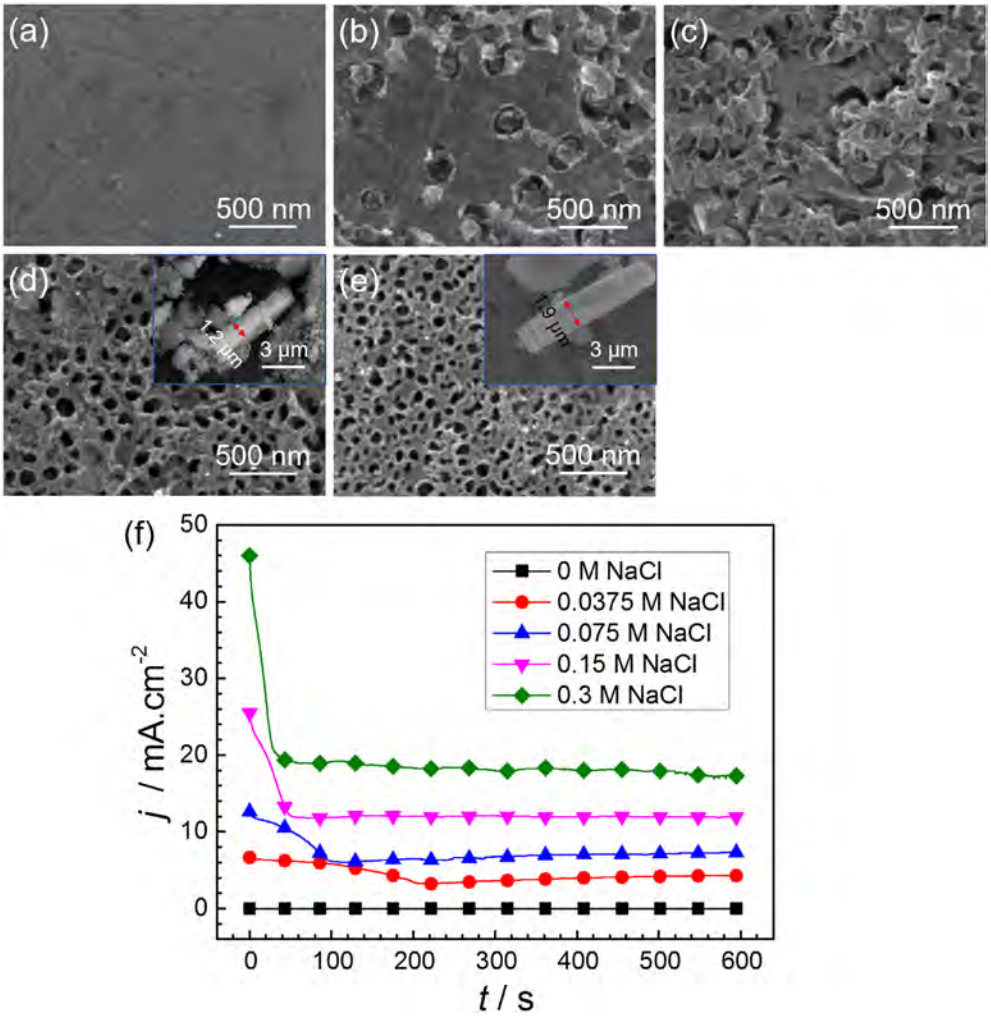

Fig. 1. (a)–(e) Surface FE-SEM images of the samples anodized at 10 V in EG containing 5.0 vol% H_2O and 0, 0.0375, 0.075, 0.15, and 0.3 M NaCl, respectively. The insets in (d) and (e) show the cross-sectional images of the NPFs. The thickness, indicated by red double-headed arrow, is given in each image. (f) Corresponding *j-t* curves during anodization. (For interpretation of the references to colour in this figure, the reader is referred to the web version of this article.)

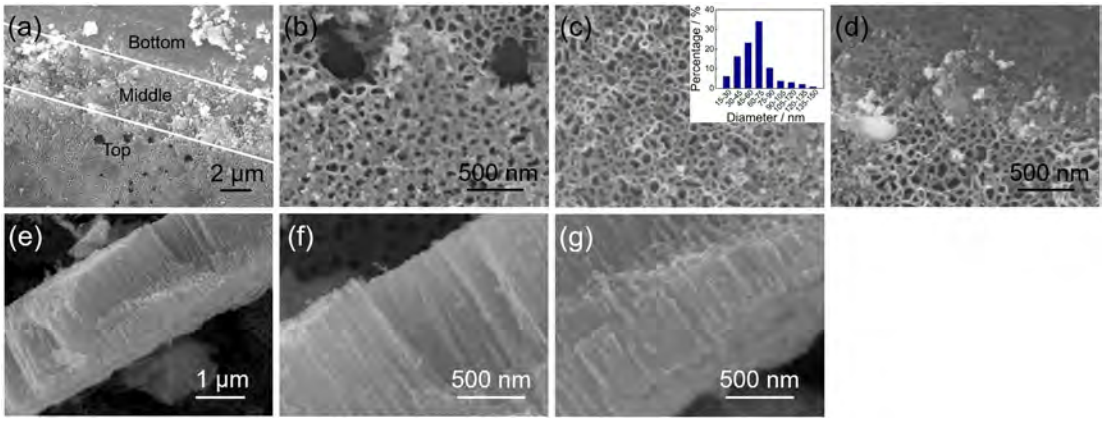

Fig. 2. Surface and cross-sectional FE-SEM images of the sample anodized at 10 V in EG containing 5.0 vol% H_2O and 0.3 M NaCl: (a) Surface image of the sample after partially peeling off the NPF by scratching. Three different regions (Top, middle, and bottom) can be identified. (b)–(d) High-magnification images corresponding to "Top", "Middle", and "Bottom" regions in (a) respectively. The inset in (c) shows the histogram of the distribution of NP diameter. (e) Cross-sectional image of the NPF. (f) and (g) High-magnification top and bottom images of the cross-section in (e).

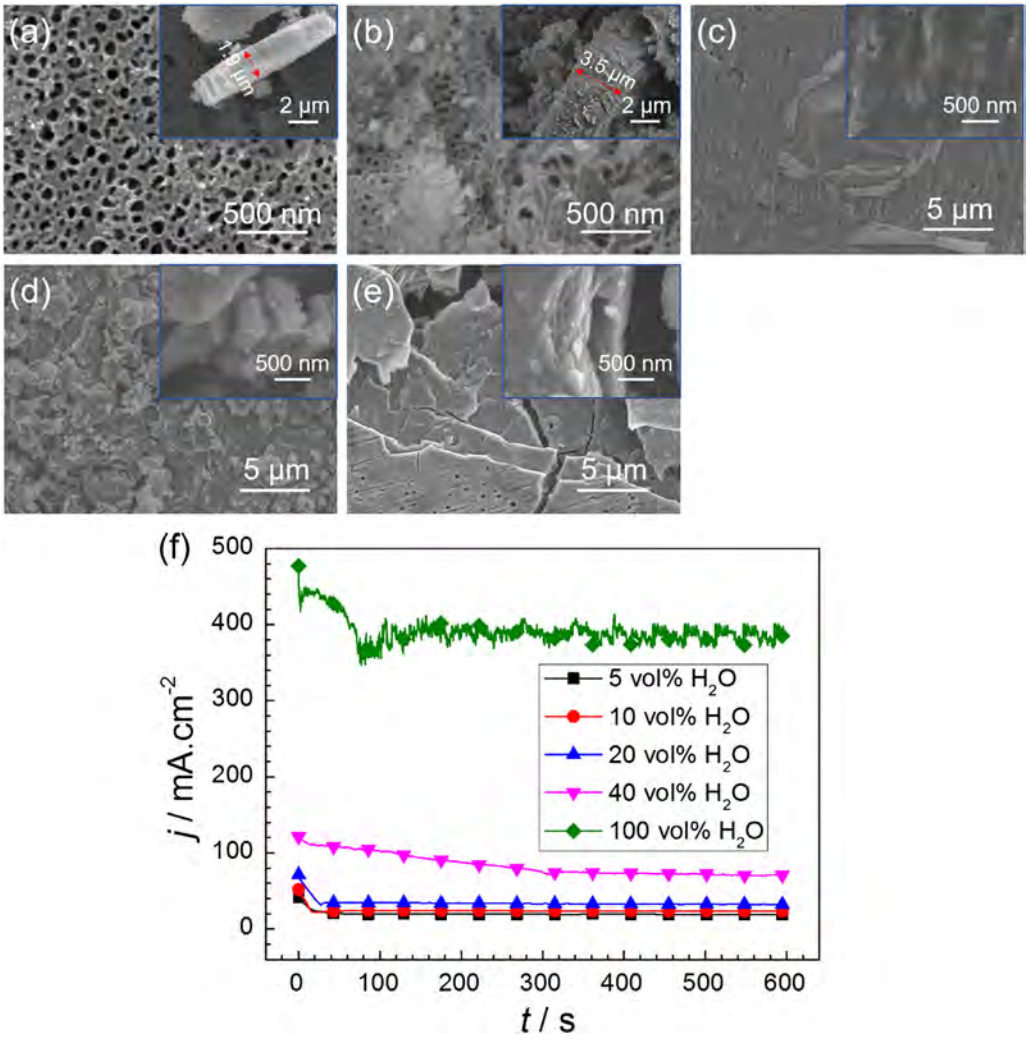

Fig. 3. (a)–(e) Surface FE-SEM images of the samples anodized at 10 V in EG containing 0.3 M NaCl and 5, 10, 20, 40, and 100 vol% H_2O, respectively. The insets in (a) and (b) show the cross-sectional images of NPFs. The thickness is indicated by a red double-headed arrow and given in each image. The insets in (c)–(e) show the corresponding high-magnification surface images. (f) Corresponding *j*–*t* curves during anodization. (For interpretation of the references to colour in this figure legend, the reader is referred to the web version of this article.)

2.4. Cytocompatibility assay

The live/dead viability/cytotoxicity kit for mammalian cells (Invitrogen) was used to evaluate the cytocompatibility of Ni-Ti-O NPF. Briefly, the endothelial cells (ECs, EA. hy926) were cultured in high-glucose DMEM (Gibco) containing 10 vol% fetal bovine serum (Sijiqing, China), 100 mg/ml streptomycin, and 100 units/ml penicillin in a humidified atmosphere with 5% CO_2 at 37 ± 0.1 °C. When the cultures were near confluence (80–90%), the cells were detached by trypsinization and plated on the alcohol-sterilized samples at a density of 2.0×10^4 cells/cm^2. After culturing for 1 day, the samples were rinsed with PBS and then 50 μl of the live/dead staining solution was added onto the sample and incubated for 40 min at room temperature in darkness, followed by rinsing with PBS and observation by confocal laser scanning microscopy (CLSM, C2 Plus, Nikon).

3. Results

3.1. Sample preparation and characterization

The influence of the NaCl concentration in the electrolyte on anodization of the NiTi alloy is investigated. As shown in Fig. 1(a), absence of the NaCl leads to a surface morphology similar to that of the mirror polished NiTi alloy. A low NaCl concentration (0.0375 M) generates sparse nanopits on its surface (Fig. 1(b)) and a larger concentration of 0.075 M produces dense ones (Fig. 1(c)). NPF can be observed from the surface of the NiTi alloy when the NaCl concentration is between 0.15 and 0.3 M (Figs. 1(d) and (e)). The insets in Figs. 1(d) and 1(e) show that the NPF thickness increases from 1.2 μm in 0.15 M NaCl to 1.9 μm in 0.3 M NaCl. The current density-time curves in Fig. 1(f) show that the current density is kept at zero during the time when the NaCl concentration is 0 M. Larger NaCl concentrations result in elevated initial and steady-state current densities (SSCDs) and shorter time to reach SSCDs.

Fig. 2 depicts the surface and cross-sectional FE-SEM images of the sample anodized at 10 V in EG containing 5.0 vol% H_2O and 0.3 M NaCl after partially peeling off the NPF by scratching. Three different regions, "Top", "Middle", and "Bottom", can be seen from near the scratch (Fig. 2(a)). The magnified "Top" image (Fig. 2(b)) reveals that an irregular nanoporous layer covers the surface. In the "Middle" region (Fig. 2(c)), where the surface irregular layer has been peeled off, ordered nanopores (NPs) can be clearly seen. The diameter as shown in inset of Fig. 2(c) is mainly between 60 and 75 nm. In the "Bottom" region, where NPF has been thoroughly removed, nanopits can be seen. The

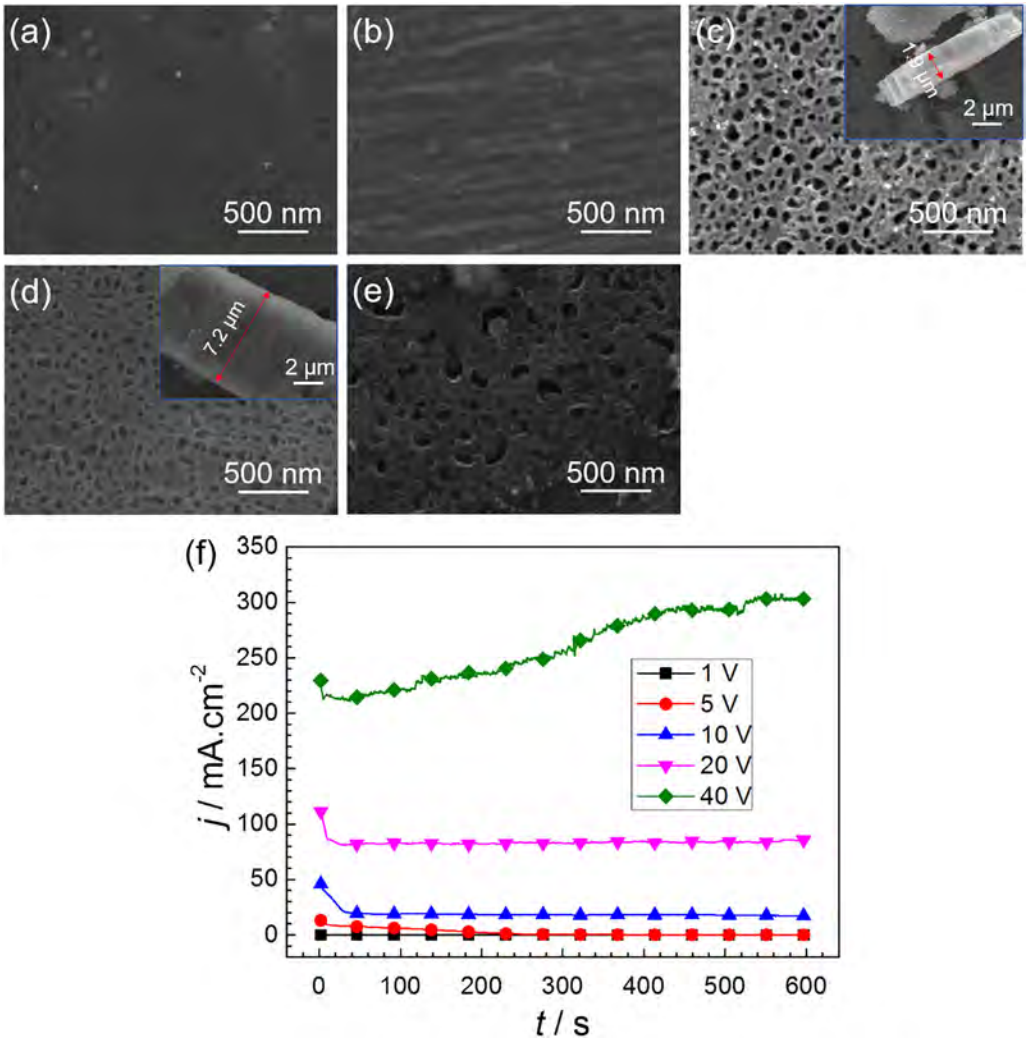

Fig. 4. (a)–(e) Surface FE-SEM images of the samples anodized in EG containing 0.3 M NaCl and 5 vol% H_2O at 1, 5, 10, 20, and 40 V, respectively. The insets in (c) and (b) show the cross-sectional images of the NPFs. The thickness is indicated by a red double-headed arrow and given in each image. (f) Corresponding *j*–*t* curves during anodization. (For interpretation of the references to colour in this figure legend, the reader is referred to the web version of this article.)

cross-sectional image (Fig. 2(e)) indicates that the NPs penetrate the oxide layer thoroughly. The high-magnification images acquired from the top (Fig. 2(f)) and bottom (Fig. 2(g)) regions of the NPF show that the walls are interconnected producing the nanoporous structure.

The H_2O content in the electrolyte is another key parameter that influences the anodization behavior of the NiTi alloy. When the H_2O concentrations are between 5 and 10 vol%, NPF are produced (Figs. 3(a) and (b)). The insets in Figs. 3(a) and (b) show that the film thickness increases from 1.9 μm in 5 vol% H_2O to 3.5 μm in 10 vol% H_2O. Further increasing the H_2O concentration generates disordered surface structures (Figs. 3(c)–(e) and the insets). The current density-time curves in Fig. 3(f) show that the SSCDs increase with H_2O contents and relatively high SSCDs with severe fluctuation are observed during anodized in 100 vol% H_2O.

The influence of the voltage on the anodization behavior of the NiTi alloy is investigated. The surface morphology of the sample anodized at 1 V (Fig. 4(a)) is similar to that of the polished NiTi alloy. Strip-like protrusions can be seen from the sample anodized at 5 V (Fig. 4(b)). When the voltage is increased to 10–20 V, NPF can be generated (Figs. 4(c) and (d)). The insets in Figs. 4(c) and (d) show that the film thickness increases from 1.9 μm at 10 V to 7.2 μm at 20 V. A higher voltage (40 V) results in the formation of an irregular porous structure (Fig. 4(e)). The corresponding current densities in Fig. 4(f) vary in a voltage-dependent manner. Generally, a high voltage results in a large current density. When an anodization voltage of 1 V is used, the current density is zero during the time recorded. When the voltage is 5–20 V, the current density is initially at a relatively high level and gradually reaches a steady value. The time to reach SSCD decreases as the anodization voltage is increased and when anodization voltage reaches 40 V, SSCD cannot be achieved.

The influence of anodization time on the NP length is presented in Fig. 5. The NPF thickens with anodization time (Figs. 5(a)-(f)) and its thickness as a function of anodization time is shown in Fig. 5(g). The growth rate is almost constant in the first 200 min and then decreases gradually with time. The NPF thickness reaches 129 μm after anodization for 24 h.

The microstructure of the NPF is examined by TEM (Figs. 6(a)-(c)). The low-magnification image (Fig. 6(a)) shows a nanoporous structure and the HR-TEM image (Fig. 6(b)) shows that the atoms in the film are disordered thus indicating its amorphous structure which is also corroborated by the SAED pattern (Fig. 6(c)). EDS (Fig. 6(d)) shows the existence of five elements, Ti, Ni, O, Cl, and C, in the NPF. The concentrations are 10.89 at.%, 1.99 at.%, 60.72 at.%, 1.97 at.%, and 25.4 at.%, respectively. The presence of Cl may be ascribed to the NaCl in the electrolyte and C may come from the EG. The results show that NPF is composed of mainly Ni, Ti, and O and are designated as Ni-Ti-O NPF.

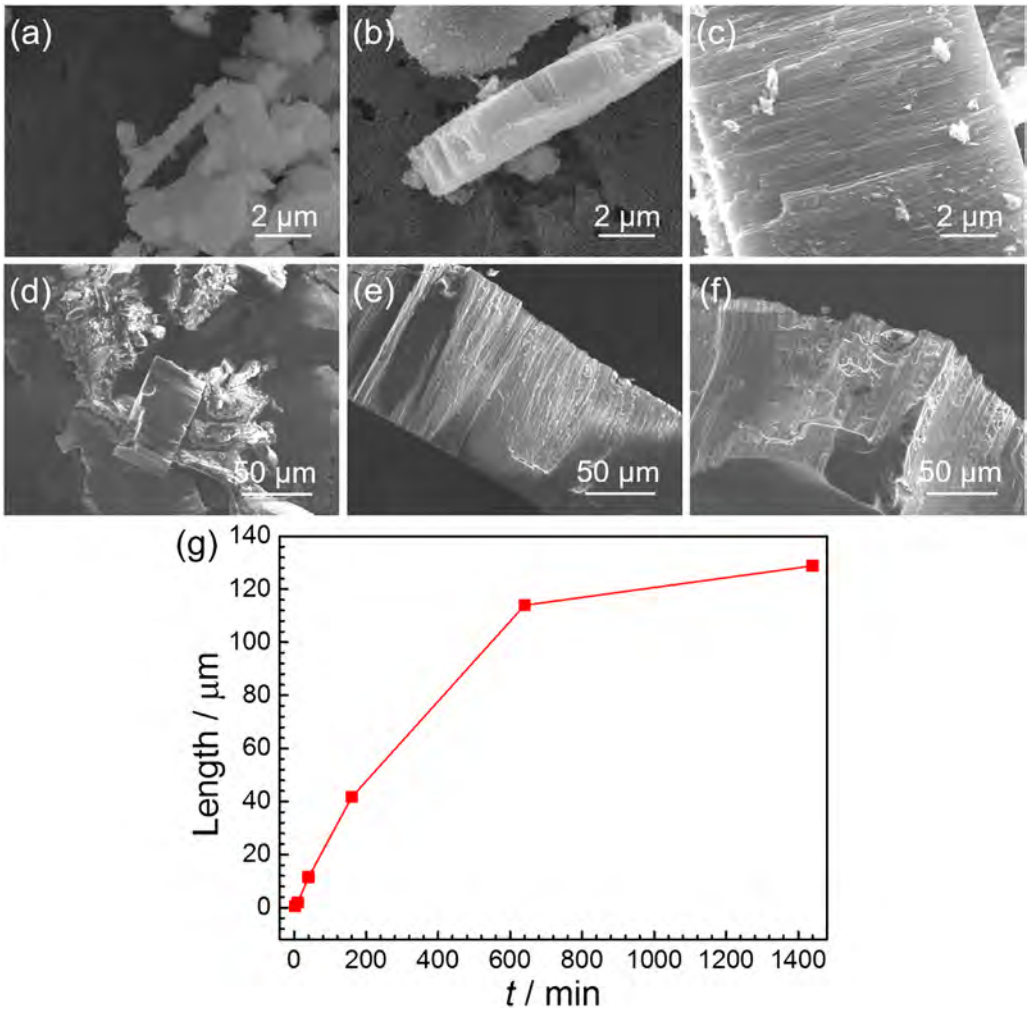

Fig. 5. (a)–(f) Cross-sectional FE-SEM images of the NPFs anodized at 10 V in EG containing 5.0 vol% H_2O and 0.3 M NaCl for 2.5, 10, 40, 160, 640, and 1440 min. (g) NPF thickness as a function of anodization time.

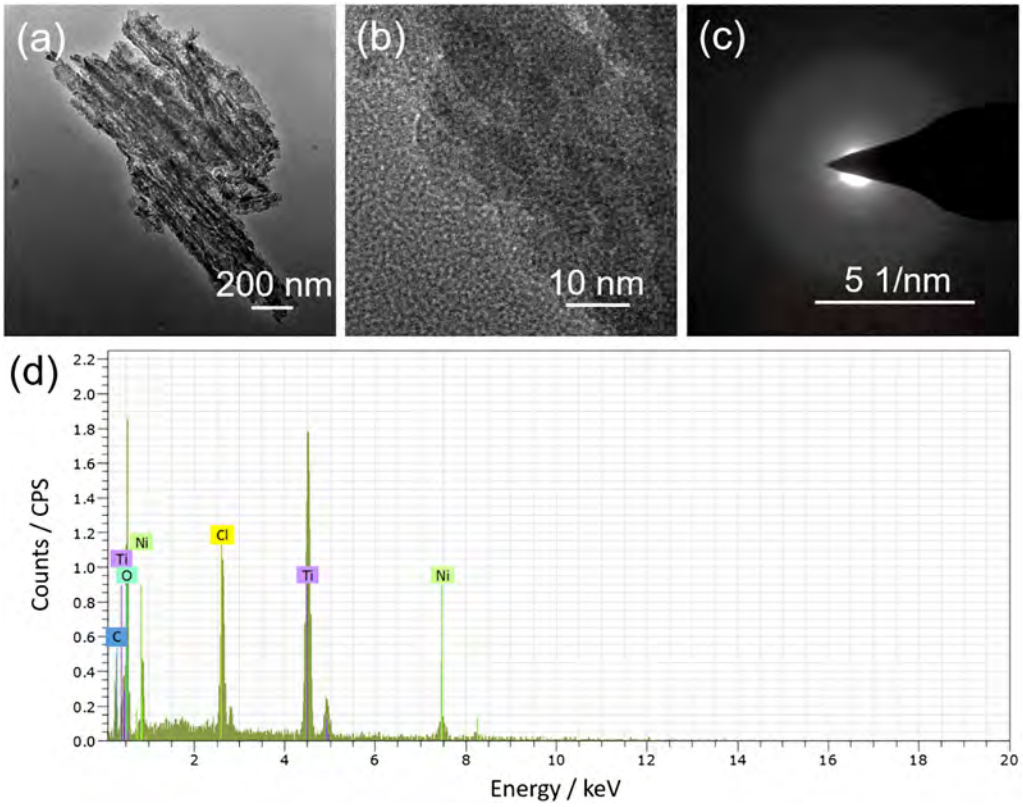

Fig. 6. TEM micrographs of the NPF anodized at 10 V in EG containing 5.0 vol% H_2O and 0.3 M NaCl: (a) TEM image; (b) HR-TEM image; (c) Selected-area electron diffraction pattern; (d) EDS spectrum of the NPF.

3.2. Influence of H^+ on anodic growth of Ni-Ti-O NPF

To investigate the influence of H^+ in the electrolyte on the anodization behavior of the Ni-Ti-O NPF, identical NaCl and HCl concentrations are used in the electrolyte and the same experimental conditions are used to anodize the NiTi alloy. Irregular and large NPF (Fig. 7(a)) 1.9 μm in thickness (Fig. 7(b)) can be observed from the sample anodized in the absence of H^+ (electrolyte containing 0.3 M NaCl). In contrast, The NPF (Fig. 7(d)) with a thickness of 5.1 μm (Fig. 7(e)) are produced in the presence of H^+ (electrolyte containing 0.3 M HCl). The high-magnification cross-sectional images (Figs. 7(c) and (f)) indicate that H^+ has little influence on the cross-sectional morphology of the NPFs. The current density-time curves (Fig. 7(g)) show that SSCD value of the sample anodized in HCl-containing electrolyte is higher than that of anodized in NaCl-containing electrolyte, namely H^+ in the electrolyte can elevate SSCD value of the sample during anodization.

3.3. Specificity of the electrolyte in anodization of the NiTi alloy

The specificity of the electrolyte in anodic growth of the NPF on the NiTi alloy is evaluated by anodizing pure Ti, pure Ni, and the NiTi alloy under identical experimental conditions. Anodization of pure Ti only generates irregular cavities at the micro level (Figs. 8(a)-(c)) and anodization of pure Ni fails to produce a well-defined surface structure (Figs. 8(d)-(f)). In contrast, anodization of the NiTi alloy under the same conditions produces uniform NPF (Figs. 8(g)-(i)). The current density-time curves (Fig. 8(j)) show that although the SSCD value of pure Ti is lower than that of pure Ni, both of them are larger than that of the NiTi alloy.

3.4. Corrosion behavior, Ni release, and cytocompatibility

Fig. 9 shows the potentiodynamic polarization curves of the untreated and anodized NiTi samples and Table 1 summarizes the electrochemical parameters determined by the Tafel extrapolation method. The NiTi alloy and NPF-3.5 μm possess similar corrosion current densities, which are slightly higher than that of NPF-1.9 μm. The amounts of Ni^{2+} released from the NiTi alloy, NPF-1.9 μm, and NPF-3.5 μm, detected by ICP-MS, are 20.85 ng/cm^2/day, 1.37 μg/cm^2/day, and 3.96 μg/cm^2/day, respectively.

The fluorescence images of live/dead staining of ECs are presented in Fig. 10. Only bright green fluorescence can be observed from the NiTi alloy and NPF-1.9 μm (Figs. 10(a) and (b)), suggesting both of them can well support cell growth. In contrast, NPF-3.5 μm behaves severe cytotoxicity as shown by the dim green and red fluorescence (Fig. 10(c)).

4. Discussion

Ordered Ni-Ti-O NPF can be fabricated in an electrolyte composed of EG, H_2O, and HCl [35] and the present study shows that it can also be produced in the electrolyte composed of EG, H_2O, and NaCl thus highlighting the role of Cl^- in anodic growth of Ni-Ti-O NPF. However, the NPF fabricated in the NaCl-containing electrolyte is much thinner than that in the HCl-containing electrolyte, suggesting the possible roles of cations (Na^+ and H^+) in anodic growth of the NPF. Generally, Na^+ does not participate in the electrochemical reactions and may have little influence on the anodization behavior of the NiTi alloy. Owing to the successful fabrication of TiO_2 NTs by anodization in aqueous solutions containing HF [2], H^+ in the electrolyte is believed to be a key reason to shorten the tube length [36]. Consequently, to lengthen the NTs, NH_4F has been used to substitute HF in order to eliminate the

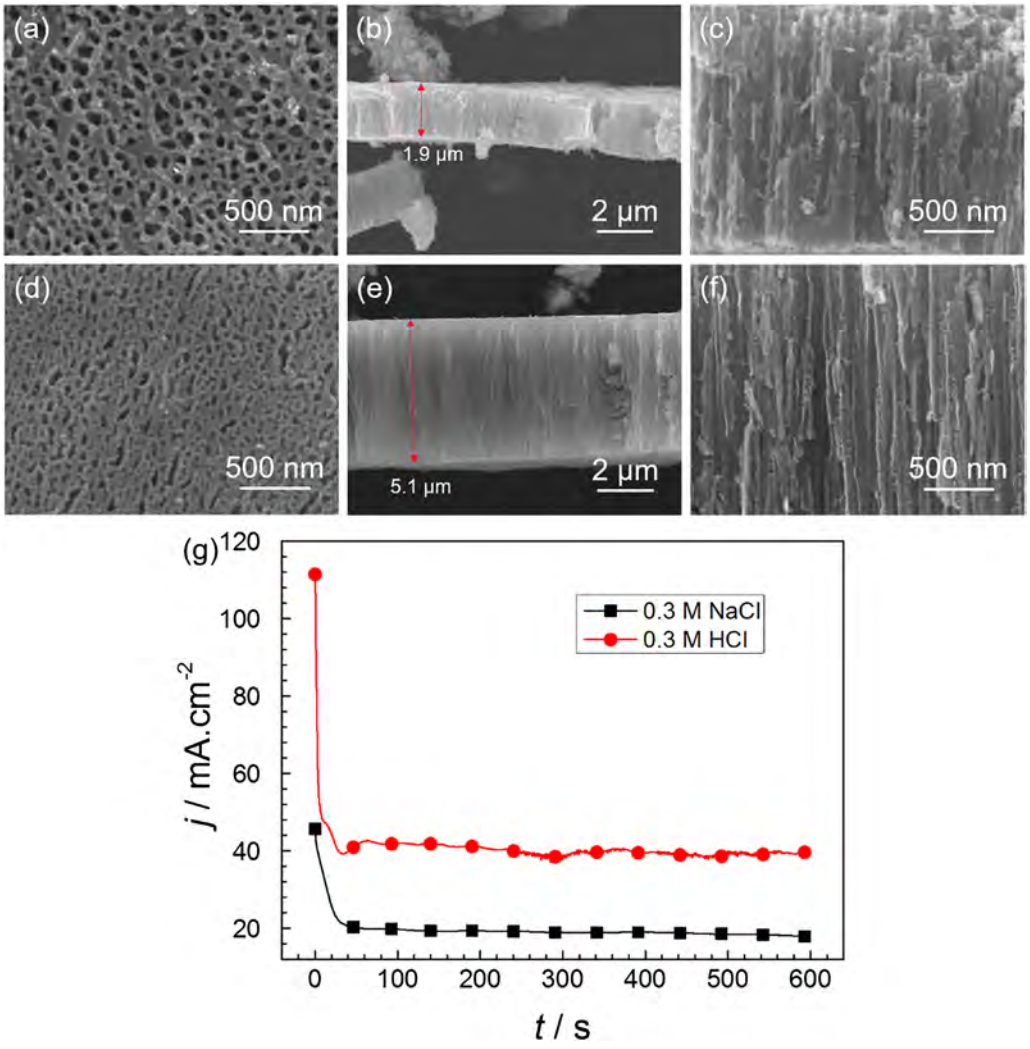

Fig. 7. Influence of H^+ in the electrolyte on anodization of the NiTi alloy: (a) Surface, (b) Low-magnification, and (c) High-magnification cross-sectional FE-SEM images of the NPF fabricated in EG containing 0.3 M NaCl and 5 vol% H_2O at 10 V. (d) Surface, (e) Low-magnification, and (f) High-magnification cross-sectional FE-SEM images of the NPF prepared in EG containing 0.3 M HCl and 5 vol% H_2O at 10 V. (g) Variation of current densities as a function of anodization time.

side effect of H^+ on the tube length [37]. However, the present work shows that H^+ in EG accelerates anodic growth of the Ni-Ti-O NPF. The possible mechanism is described in the following. It is well known that anodic fabrication of a nanoporous/tubular structure is ascribed to the balance between anodic growth of the oxide film and etching of the oxide film by aggressive ions. Initially, a compact oxide layer composed of TiO_2 and NiO is formed according to the following equations [36]:

$$Ti + 2H_2O \rightarrow TiO_2 + 4H + 4e^- \quad (1)$$

$$Ni + H_2O \rightarrow NiO + 2H + 2e^-. \quad (2)$$

Immediately, Cl^- in the electrolyte attacks the newly formed oxide layer to generate the nanoporous structure by the following reactions [33]:

$$TiO_2 + 4H^+ + 6Cl^- \rightarrow TiCl_6^{2-} + 2H_2O \quad (3)$$

$$NiO + 2H^+ + 4Cl^- \rightarrow NiCl_4^{2-} + H_2O. \quad (4)$$

It can be seen that Eqs. (1) and (2) produce H^+ whereas Eqs. (3) and (4) consume H^+. If H^+ is preexistent in the electrolyte (using of HCl-containing electrolyte), it will retard oxide formation through slowing Eqs. (1) and (2) and facilitate oxide dissolution through accelerating Eqs. (3) and (4), which will make the bottom oxide layer thin and in turn facilitate mass transport at the electrode/electrolyte interface thus accelerating the electrochemical process and thickening the NPF compared to the situation in the absence of H^+.

To fabricate a self-organized nanoporous/tubular structure on different metals and their alloys by anodization, different experimental conditions, especially composition of the electrolyte, are usually required. For example, TiO_2 NTs can be grown on pure Ti in aqueous and organic electrolytes, while ordered Ni-Ti-O NTs can only be fabricated on NiTi alloy in an organic electrolyte [30,31]. Similarly, the present work indicates that the electrolyte for the anodic growth of NPF on the NiTi alloy may not be suitable for pure Ti and Ni. The possible reason may be the mismatch between the electro-oxidation of the constituent elements and dissolution of oxide by attack of Cl^-.

NiTi alloy is used biomedically on account of its unique mechanical and other desirable properties. Nevertheless, Ni^{2+} release from the bulk material may raise safety concerns. It is generally recognized that the release of Ni^{2+} is ascribed to spontaneously electrochemical corrosion, which can be evaluated by corrosion current density. However, in the present case Ni^{2+} release level and corrosion current density cannot be well matched. A possible explanation may be high chemical solubility

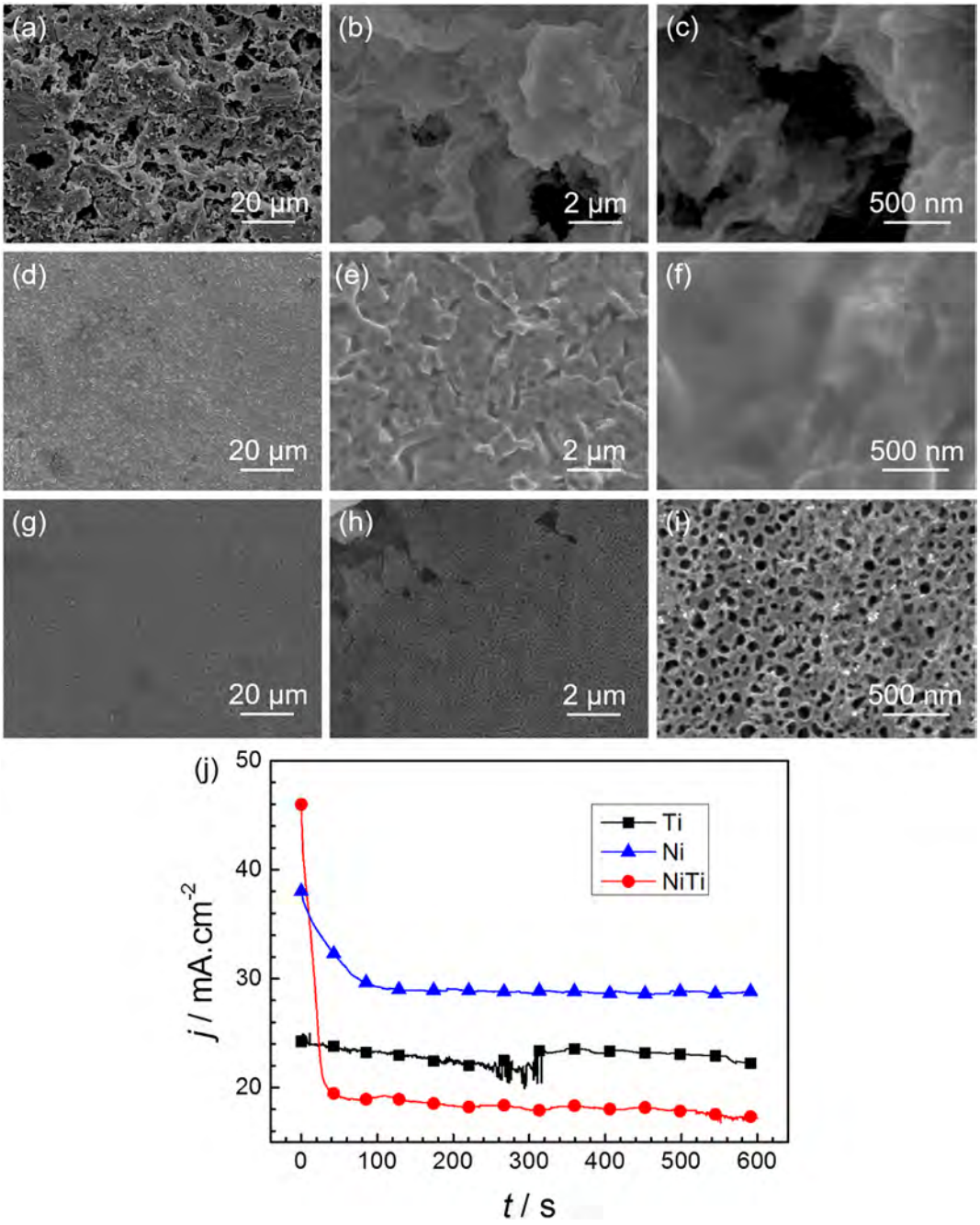

Fig. 8. Anodization behavior of pure Ti, pure Ni, and the NiTi alloy in EG containing 0.3 M NaCl and 5.0 vol% H_2O at 10 V: (a) Low, (b) Medium, and (c) High-magnification FE-SEM images of the anodized pure Ti. (d) Low, (e) Medium, and (f) High-magnification FE-SEM images of the anodized pure Ni alloy. (g) Low, (h) Medium, and (i) High-magnification FE-SEM images of the anodized NiTi alloy. (j) Variation of current densities as a function of anodization time.

of Ni species in the NPF in aqueous solution, which cannot be reflected by electrochemical tests. Because of the use of NaCl in the electrolyte during anodization, partial Ni in the NPF may be in the form of water-soluble $NiCl_2$. After in contact with PBS or cell culture medium, it will then spontaneously dissolves in it, leading relatively high Ni^{2+} concentration in the solution. Although Ni is an essential trace element for human beings, previous works have shown that when Ni^{2+} concentration in the culture medium reaches up to 0.2 mmol/l it is toxic to endothelial and fibroblast cells [38,39]. Even though the toxic threshold amount of Ni^{2+} to osteoblasts is still unclear, it is expected near the value of 0.2 mmol/l. Based on the release amount of Ni^{2+} from the NPF, its value in the culture medium for NPF-1.9 μm and NPF-3.5 μm is calculated to be approximate 0.023 and 0.068 mmol/l respectively, which are much smaller than the expected threshold value (0.2 mmol/l). Accordingly, the influence of Ni^{2+} release on the cytocompatibility of the NPF may be negligible. Another factor that may influence the cytocompatibility of the NPF is surface morphology. Previous works have demonstrated that TiO_2 NTs with large diameters can suppress cell adhesion and proliferation through inhibiting integrin clustering and focal contact formation [9,36]. As can be seen in Fig. 3, the surface of NPF-3.5 μm is rougher than that of NPF-1.9 μm, which may also suppress cell functions in the same way as that of large TiO_2 NTs. Nonetheless, more works should be conducted to clarify the respective roles of Ni^{2+} release and surface morphology on the cytocompatibility of the NPFs.

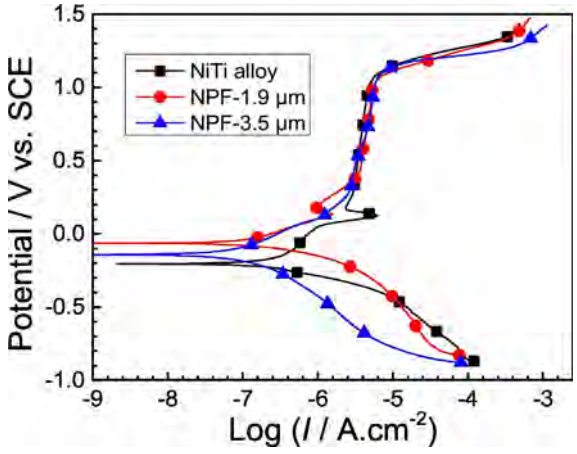

Fig. 9. Potentiodynamic polarization curves of the untreated and anodized NiTi samples - NiTi alloy: untreated NiTi sample. NPF-1.9 μm: NPF thickness = 1.9 μm. It is produced in EG containing 0.3 M NaCl and 5 vol% H_2O at 10 V. NPF-3.5 μm: NPF thickness = 3.5 μm. It is prepared in EG containing 0.3 M NaCl and 10 vol% H_2O at 10 V.

Table 1
Corrosion potentials (E_{corr}), current densities (I_{corr}), and cathodic Tafel slopes (β_c) of the Ni-Ti-O NPFs derived from the polarization curves.

Sample	E_{corr}/V vs. SCE	I_{corr}/A·cm^{-2}	βc/V·decade^{-1}
NiTi alloy	−0.21	1.35×10^{-7}	−0.095
NPF-1.9 μm	−0.06	1.90×10^{-7}	−0.122
NPF-3.5 μm	−0.14	1.39×10^{-7}	−0.329

5. Conclusion

Amorphous Ni-Ti-O NPFs with diameters between 60 and 75 nm are produced anodically in ethylene glycol containing 5–10 vol% H_2O and 0.15–0.3 M NaCl at 10–20 V. Under the optimal conditions, the thickness of NPF can reach up to 129 μm. A comparison between the anodic growth of Ni-Ti-O NPFs in NaCl-containing and HCl-containing electrolytes under similar conditions indicates that H^+ accelerate the process. Since NPF cannot be produced on pure Ti and Ni under similar experimental conditions, the electrolyte is specific for the anodic growth of NPF on the NiTi alloy. Constructing Ni-Ti-O NPF has little influence on the corrosion behavior but increases Ni release of the NiTi alloy. The NPF with 1.9 μm in thickness show good cytocompatibility.

Acknowledgements

This work was jointly supported by the National Natural Science Foundation of China (31400815, 51671140), Scientific and Technological Innovation Programs of Higher Education Institutions in Shanxi (201626), Hong Kong Research Grants Council (RGC)-General Research Funds (GRF) No. CityU 11301215, and City University of Hong Kong Applied Research Grant (ARG) No. 9667122.

References

[1] M.S. Sander, L.S. Tan, Nanoparticle arrays on surfaces fabricated using anodic alumina films as templates, Adv. Funct. Mater. 13 (2003) 393–397.
[2] V. Zwilling, E. Darque-Ceretti, A. Boutry-Forveille, D. David, M.-Y. Perrin, M. Aucouturier, Structure and physicochemistry of anodic oxide films on titanium and TA6V alloy, Surf. Interface Anal. 27 (1999) 629–637.
[3] K. Zhu, N.R. Neale, A. Miedaner, A.J. Frank, Enhanced charge-collection efficiencies and light scattering in dye-sensitized solar cells using oriented TiO_2 nanotubes arrays, Nano Lett. 7 (2007) 69–74.
[4] Q. Zheng, B. Zhou, J. Bai, L. Li, Z. Jin, J. Zhang, J. Li, Y. Liu, W. Cai, X. Zhu, Self-organized TiO_2 nanotube array sensor for the determination of chemical oxygen demand, Adv. Mater. 20 (2008) 1044–1049.
[5] K.-S. Mun, S.D. Alvarez, W.-Y. Choi, M.J. Sailor, A stable, label-free optical interferometric biosensor based on TiO_2 nanotube arrays, ACS Nano 4 (2010) 2070–2076.
[6] G.K. Mor, K. Shankar, M. Paulose, O.K. Varghese, C.A. Grimes, Enhanced photocleavage of water using titania nanotube arrays, Nano Lett. 5 (2005) 191–195.
[7] G.F. Ortiz, I. Hanzu, P. Knauth, P. Lavela, J.L. Tirado, T. Djenizian, TiO_2 nanotubes manufactured by anodization of Ti thin films for on-chip li-ion 2D microbatteries, Electrochim. Acta 54 (2009) 4262–4268.
[8] O.K. Varghese, M. Paulose, T.J. LaTempa, C.A. Grimes, High-rate solar photocatalytic conversion of CO_2 and water vapor to hydrocarbon fuels, Nano Lett. 9 (2009) 731–737.
[9] J. Park, S. Bauer, K.A. Schlegel, F.W. Neukam, K. von der Mark, P. Schmuki, TiO_2 nanotube surfaces: 15 nm—an optimal length scale of surface topography for cell adhesion and differentiation, Small 5 (2009) 666–671.
[10] Y.C. Nah, I. Paramasivam, P. Schmuki, Doped TiO_2 and TiO_2 nanotubes: synthesis and applications, ChemPhysChem 11 (2010) 2698–2713.
[11] H. Jha, R. Hahn, P. Schmuki, Ultrafast oxide nanotube formation on TiNb, TiZr and TiTa alloys by rapid breakdown anodization, Electrochim. Acta 55 (2010) 8883–8887.
[12] H. Tsuchiya, T. Akaki, J. Nakata, D. Terada, N. Tsuji, Y. Koizumi, Y. Minamino, P. Schmuki, S. Fujimoto, Anodic oxide nanotube layers on Ti–ta alloys: substrate composition, microstructure and self-organization on two-size scales, Corros. Sci. 51 (2009) 1528–1533.
[13] S.N. Basahel, K. Lee, R. Hahn, P. Schmuki, S.M. Bawaked, S.A. Al-Thabaiti, Self-decoration of Pt metal particles on TiO_2 nanotubes used for highly efficient photocatalytic H_2 production, Chem. Commun. 50 (2014) 6123–6125.
[14] K. Lee, R. Hahn, M. Altomare, E. Selli, P. Schmuki, Intrinsic au decoration of growing TiO_2 nanotubes and formation of a high-efficiency photocatalyst for H_2 production, Adv. Mater. 25 (2013) 6133–6137.
[15] R. Hang, X. Huang, L. Tian, Z. He, B. Tang, Preparation, characterization, corrosion behavior and bioactivity of Ni_2O_3-doped TiO_2 nanotubes on NiTi alloy, Electrochim. Acta 70 (2012) 382–393.
[16] R. Hang, Y. Zhao, L. Bai, Y. Liu, A. Gao, X. Zhang, X. Huang, B. Tang, P.K. Chu, Fabrication of irregular-layer-free and diameter-tunable Ni–Ti–O nanopores by anodization of NiTi alloy, Electrochem. Commun. 76 (2017) 10–14.
[17] P. Roy, C. Das, K. Lee, R. Hahn, T. Ruff, M. Moll, P. Schmuki, Oxide nanotubes on Ti−Ru alloys: strongly enhanced and stable photoelectrochemical activity for water splitting, J. Am. Chem. Soc. 133 (2011) 5629–5631.
[18] R. Hang, A. Gao, X. Huang, X. Wang, X. Zhang, L. Qin, B. Tang, Antibacterial activity and cytocompatibility of cu–Ti–O nanotubes, J. Biomed. Mater. Res. A 102 (2014) 1850–1858.
[19] M. Zong, L. Bai, Y. Liu, X. Wang, X. Zhang, X. Huang, R. Hang, B. Tang, Antibacterial ability and angiogenic activity of cu-Ti-O nanotube arrays, Mater. Sci. Eng. C 71 (2017) 93–99.
[20] I. Paramasivam, Y.C. Nah, C. Das, N.K. Shrestha, P. Schmuki, WO_3/TiO_2 nanotubes with strongly enhanced photocatalytic activity, Chem.–Eur. J. 16 (2010) 8993–8997.
[21] A. Gao, R. Hang, X. Huang, L. Zhao, X. Zhang, L. Wang, B. Tang, S. Ma, P.K. Chu, The effects of titania nanotubes with embedded silver oxide nanoparticles on bacteria and osteoblasts, Biomaterials 35 (2014) 4223–4235.

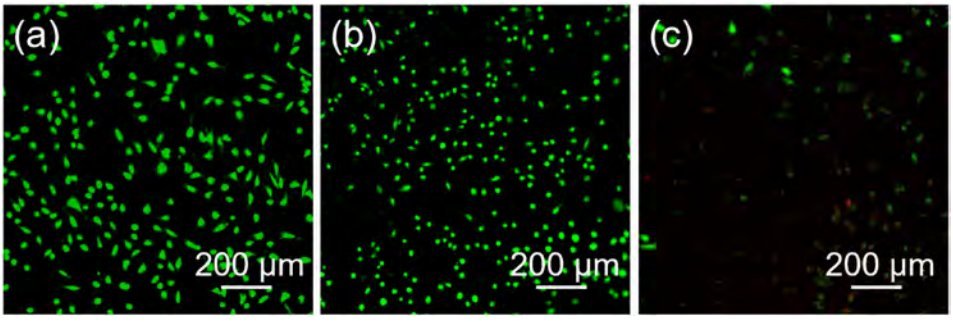

Fig. 10. Fluorescence images after live/dead staining of the ECs: (a) NiTi alloy, (b) NPF-1.9 μm, and (c) NPF-3.5 μm. The green colour represents live cells and red colour show dead cells. (For interpretation of the references to colour in this figure, the reader is referred to the web version of this article.)

[22] Y. Chen, A. Gao, L. Bai, Y. Wang, X. Wang, X. Zhang, X. Huang, R. Hang, B. Tang, P.K. Chu, Antibacterial, osteogenic, and angiogenic activities of $SrTiO_3$ nanotubes embedded with Ag_2O nanoparticles, Mater. Sci. Eng. C 75 (2017) 1049–1058.
[23] P. Agarwal, I. Paramasivam, N.K. Shrestha, P. Schmuki, MoO_3 in self-organized TiO_2 nanotubes for enhanced photocatalytic activity, Chem.-Asian J. 5 (2010) 66–69.
[24] L. Benea, E. Danaila, P. Ponthiaux, Effect of titania anodic formation and hydroxyapatite electrodeposition on electrochemical behaviour of Ti–6Al–4V alloy under fretting conditions for biomedical applications, Corros. Sci. 91 (2015) 262–271.
[25] J.-H. Kim, K. Zhu, Y. Yan, C.L. Perkins, A.J. Frank, Microstructure and pseudocapacitive properties of electrodes constructed of oriented NiO-TiO_2 nanotube arrays, Nano Lett. 10 (2010) 4099–4104.
[26] H. He, G. Ke, P. He, J. Liang, F. Dong, Ordered NiO–TiO_2 nanotube arrays as an efficient catalyst support for methanol oxidation, Phys. Status Solidi A 212 (2015) 2085–2090.
[27] Z. Li, D. Ding, Q. Liu, C. Ning, X. Wang, Ni-doped TiO_2 nanotubes for wide-range hydrogen sensing, Nanoscale Res. Lett. 9 (2014) 1–9.
[28] R. Hang, Y. Liu, A. Gao, L. Bai, X. Huang, X. Zhang, N. Lin, B. Tang, P.K. Chu, Highly ordered Ni–Ti–O nanotubes for non-enzymatic glucose detection, Mater. Sci. Eng. C 51 (2015) 37–42.
[29] R. Hang, Y. Liu, S. Liu, L. Bai, A. Gao, X. Zhang, X. Huang, B. Tang, P.K. Chu, Size-dependent corrosion behavior and cytocompatibility of Ni–Ti–O nanotubes prepared by anodization of biomedical NiTi alloy, Corros. Sci. 103 (2016) 173–180.
[30] P.P. Lee, T.A. Desai, Nitinol-based nanotubular arrays with controlled diameters upregulate human vascular cell ECM production, ACS Biomater Sci. Eng. 2 (2016) 409–414.
[31] R. Hang, Y. Liu, L. Zhao, A. Gao, L. Bai, X. Huang, X. Zhang, B. Tang, P.K. Chu, Fabrication of Ni-Ti-O nanotube arrays by anodization of NiTi alloy and their potential applications, Sci. Rep. 4 (2014) 7547.
[32] X. Chen, M. Schriver, T. Suen, S.S. Mao, Fabrication of 10 nm diameter TiO_2 nanotube arrays by titanium anodization, Thin Solid Films 515 (2007) 8511–8514.
[33] N.K. Allam, C.A. Grimes, Formation of vertically oriented TiO_2 nanotube arrays using a fluoride free HCl aqueous electrolyte, J. Phys. Chem. C 111 (2007) 13028–13032.
[34] N.K. Allam, K. Shankar, C.A. Grimes, Photoelectrochemical and water photoelectrolysis properties of ordered TiO_2 nanotubes fabricated by Ti anodization in fluoride-free HCl electrolytes, J. Mater. Chem. 18 (2008) 2341–2348.
[35] R. Hang, M. Zong, L. Bai, A. Gao, Y. Liu, X. Zhang, X. Huang, B. Tang, P.K. Chu, Anodic growth of ultra-long Ni-Ti-O nanopores, Electrochem. Commun. 71 (2016) 28–32.
[36] P. Roy, S. Berger, P. Schmuki, TiO_2 nanotubes: synthesis and applications, Angew. Chem. Int. Ed. 50 (2011) 2904–2939.
[37] J.M. Macak, H. Tsuchiya, L. Taveira, S. Aldabergerova, P. Schmuki, Smooth anodic TiO_2 nanotubes, Angew. Chem. Int. Ed. 44 (2005) 7463–7465.
[38] R. Hang, M. Zhang, S. Ma, P.K. Chu, Biological response of endothelial cells to diamond-like carbon-coated NiTi alloy, J. Biomed. Mater. Res. A 100 (2012) 496–506.
[39] X. Lü, X. Bao, Y. Huang, Y. Qu, H. Lu, Z. Lu, Mechanisms of cytotoxicity of nickel ions based on gene expression profiles, Biomaterials 30 (2009) 141–148.